THE JOURNAL OF PHYSICAL CHEMISTRY C
A JOURNAL OF THE AMERICAN CHEMICAL SOCIETY

pubs.acs.org/JPCC
Article

Inorganic Solid Electrolyte Interphase Engineering Rationales Inspired by Hexafluorophosphate Decomposition Mechanisms

Dacheng Kuai and Perla B. Balbuena*

Cite This: J. Phys. Chem. C 2023, 127, 1744−1751

Read Online

ACCESS | Metrics & More | Article Recommendations | Supporting Information

ABSTRACT: Solid electrolyte interphase (SEI) engineering is an efficient approach to enhancing the cycling performance of lithium metal batteries. Lithium hexafluorophosphate ($LiPF_6$) is a popular electrolyte salt. Mechanistic insights into its degradation pathways near the lithium metal anode are critical in modifying the battery electrolyte and SEI. In this work, we elucidate plausible reaction pathways in multiple representative electrolyte systems. Through ab initio molecular dynamics simulations, lithiation and electron transfer are identified as the triggering factors for $LiPF_6$ degradation. Meanwhile, we find that lithium morphology and charge distribution substantially impact the interfacial dissociation pathways. Thermodynamic evaluation of the solvation effects shows that higher electrolyte dielectric constant and lithiation extent profoundly assist the $LiPF_6$ decomposition. These findings offer quantitative thermodynamic and electronic structure information, which promotes rational SEI engineering and electrolyte tuning for lithium metal anode performance enhancement.

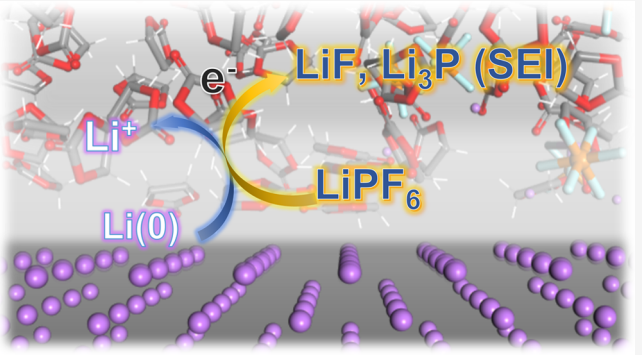

INTRODUCTION

Current commercially available lithium-ion batteries are approaching their theoretical limits, while the electronics market still urges further energy capacity extension.[1] The lithium metal battery (LMB) is a promising technical route for next-generation energy storage devices.[2] The cycling efficiency and safety risk control on the battery anode are the primary technical obstacles that hinder LMB commercialization.[3] Solid electrolyte interphase (SEI) formed on the anode surface regulates Li^+ ion migration and deposition, which is critical in minimizing lithium dendrite and whisker formation.[4] Therefore, the battery's electrochemical performance is tightly bonded with SEI morphology and composition.[5]

Fluorination has been suggested as an efficient strategy in battery electrolytes and SEI engineering.[6] The fluorine-containing electrolyte components, such as $LiPF_6$, lithium bis(fluorosulfonyl)imide (LiFSI), and fluoroethylene carbonate (FEC), experience decomposition and yield lithium fluoride nanoparticles in SEI. However, the SEI internal structures are notoriously complex to resolve due to their fragility and chemical reactiveness.[2] So far, only limited while expensive techniques such as cryo-electron microscopy are able to precisely probe the spatial distributions of SEI nanostructures, where battery disassembly is mandatory.[7] In addition, the electrolyte species also alter the solvation environment, which profoundly impacts the thermochemistry and kinetics of SEI formation reactions.[8,9] Aside from the designing principles based on empirical concepts, theoretical approaches are expected to envision the electrolyte−electrode interfacial chemistry and ion transport mechanisms.[3,10−12] Hereby, we study the reactions resulting in prevalent inorganic components in SEI from $LiPF_6$-based electrolytes. The quantitative understanding of the reaction thermodynamics may enable future multiscale simulations of the SEI formation processes.

It is inherently challenging to characterize the electrode−electrolyte interfacial chemistry at the nanoscale.[13] The SEI grows in such a highly reductive and salty environment. Despite limited experimental data available to precisely elucidate the SEI composition and formation mechanisms, many proposals depict plausible scenarios in generating SEI of LMB.[2,13] Hexafluorophosphate degradation is recognized as the primary contributor to the LiF in SEI based on this electrolyte chemistry, while few reports denote the destination of phosphorus. A trace amount of moisture in battery electrolyte can cause hydrolysis of PF_6^-, yielding POF_3 and its derivatives as detected in spectroscopic analysis.[14,15] Further information regarding the direct PF_6^- decomposition and reduction without water participation is less reported in the experimental work. The characterization of interfacial chemistry is particularly challenging in accessing delicate nanoscale

Received: November 7, 2022
Revised: December 30, 2022
Published: January 23, 2023

https://doi.org/10.1021/acs.jpcc.2c07838
J. Phys. Chem. C 2023, 127, 1744−1751

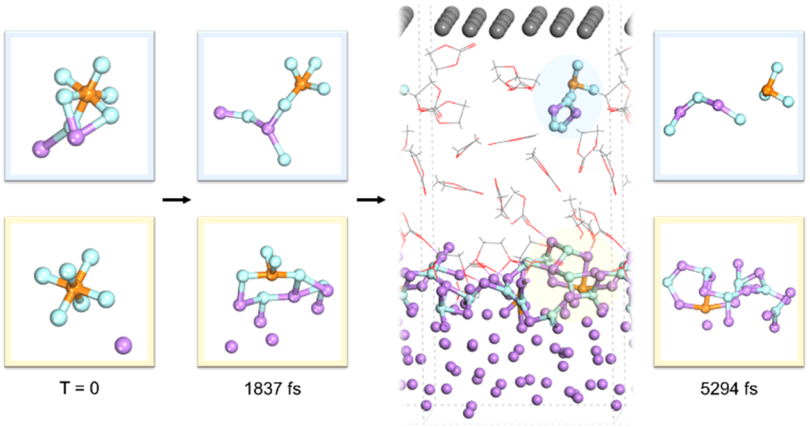

Figure 1. AIMD simulation of $LiPF_6$ decomposition on and near lithium metal surface. The initial electrolyte configuration is composed of 3 Li^+, 3 PF_6^-, 18 EC, and 1 VC structures, with a density of 1.3 g/mL. The coordinates of the top-layer He atoms (dark gray) are fixed to refrain electrolyte molecular movement from contacting the lithium layer repeated in the *z*-direction due to periodic boundary conditions. Some cluster structures are rotated for a clear perspective. Color scheme: He (gray ball); C (gray dash); H (white dash); O (red dash); Li (purple ball); P (tan ball); F (cyan ball).

surfaces.[13,16] First principles simulation is compelling in predicting the molecular behavior at the metal−liquid interface, which is fragile to atmospheric interruptions.[17] Ab initio molecular dynamics (AIMD) successfully predicts the stabilities and reductive dissociation of electrolyte solvents near metallic surfaces.[18,19]

The $LiPF_6$ degradation chemistry near the anode shows unique features. The phosphorous element usually demonstrates a singlet electronic state in stable compounds. However, some reported atomic charge analysis on the AIMD simulation shows that this rule may not apply to all cases in the $LiPF_6$ decomposition near lithium battery anode surfaces. Martinez de la Hoz et al. identified the plausible oxidation state pathway on the silicone anode surface, where the equilibrium charge state of phosphorous was identified to be −1.[20] A fully reduced phosphorous reduction product was found in the lithium metal case.[21] Both these scenarios require continuous electron uptake.

Ether-based electrolytes are mainly composed of dimethoxyethane (DME) and 1,3-dioxolane (DOL), with moderate dielectric constants (ε) varying from 4 to 10.[22] High salt concentration is mandatory in maintaining the integrity of ether solvents in high voltages, despite their compatibility with lithium metal.[23,24] The commonly used carbonate solvents, including ethylene carbonate (EC), propylene carbonate (PC), and vinylene carbonate (VC), create a solvation environment with much higher dielectric constants and unique solvation structures.[22] In the electrolyte environment with a positive dielectric constant, the direct electron tunneling probability decays exponentially with respect to particle−metal-surface distance. Consequently, electron-induced reactions usually occur via complex charge transport mechanisms that manipulate the corresponding redox reaction rate.[25] The ion−solvent interactions are one of the most important factors in bottom-up LMB development.[26] The beginning stages of phase separation and ionic nucleation in forming SEI have been reported in previous molecular dynamics (MD) and AIMD studies.[27−29] A longer simulation time scale may compensate for this issue by implementing high-quality ab initio thermodynamic information in kinetic Monte Carlo (kMC) simulations.[30] Beyond elucidating the underlying chemical processes, we aim to contribute toward data-driven LMB electrolyte and SEI engineering from the electrolyte solvation and anode morphology perspectives.

COMPUTATIONAL METHODS

After creating a vacuum slab on top of the Li metal crystal surface structure, the initial configurations for AIMD were obtained by packing the geometry-optimized structures of electrolyte species in the vacuum space based on the Amorphous Cell Packing module in Materials Studio v8. In the selected configuration, relative positions of hexafluorophosphate particles were verified to include both the following conditions: (1) close contact to the Li metal surface and (2) dissolved in electrolyte while the mass center is at least 5 Å away from the lithium surface. The molar ratios of each species and the system density were further assessed to be consistent with the experimental macroscopic properties. The AIMD simulations were performed via VASP 5.4.4.[31] The Perdew−Burke−Ernzerhof (PBE) functional was used to describe the electron exchange and correlation energies within the generalized gradient approximation (GGA).[32] Electron−ion interactions were considered within the projector augmented wave (PAW) pseudopotentials.[33,34] The plane waves were extended to a cutoff energy of 520 eV. The simulations were based on an NVT ensemble at 300 K with 1-fs time step. DFT-D3 method of Grimme with the zero-damping function was implemented to correct van der Waals interaction terms.[35] The atomic Bader charges were analyzed based on the grid-based method developed by Henkelman et al.[36]

Molecular modeling was primarily conducted on the Gaussian16 package. All intermediate structures were optimized to their local minimum without imaginary vibration mode, and the corresponding free energy values were converted to the standard state of 1 M. M06-2X/aug-cc-pVDZ level of theory was employed based on the benchmark results previously reported by Han et al.[37−39] Solvation effects were evaluated based on the implicit solvation model based on density (SMD).[40] Empirical dispersion interactions were introduced in calculations.[41]

https://doi.org/10.1021/acs.jpcc.2c07838
J. Phys. Chem. C 2023, 127, 1744−1751

RESULTS AND DISCUSSION

We initially estimate the degradation energetics of $LiPF_6$ with different spin states at the molecular level, as shown in Table S1 in SI. The only free energy barrier exists at the first P−F cleavage process. However, the real SEI formation environment is much more complex than this simple model. As an example of the complexity of interfacial reactions, it has been reported that the solvent−reactant interactions at the air−liquid interface can profoundly alter the reaction thermodynamic profile, and such impact varies under different dielectric environments.[16] Similarly, many factors, including metal−electrolyte interfacial effects, solvation effects, charge transport, and lithium coordination, contribute to the $LiPF_6$ degradation reactions. Here, we apply AIMD simulations to elucidate the interfacial decomposition reactions and further quantitatively evaluate the key conditions at the molecular level.

Lithiation and Electron-Tunneling-Induced Salt Degradation. We perform AIMD simulations to reveal the ultrafast decomposition of $LiPF_6$ in different electrolyte systems. The initial configuration contained PF_6^- structures with different lithium coordination degrees and distances to the lithium metal surface. The time scale required for salt degradation varies in different solvation environments. In the cyclic carbonate-solvated system (Figure 1), the PF_6^- structures close to the lithium metal surface easily decompose within 2 ps of simulation time. Following such an event, the EC and VC structures disintegrate into carbonyl/carbon monoxide and ethylene di-carbonate (EDC). The solvent degradation pathways have been investigated in many systematic works.[42−45] In addition to the complete degradation at the electrolyte−metal interface, we also observe the partial dissociation phenomenon of $[Li_2PF_6]^+$ complex, which is located 15 Å from the lithium metal surface and 8 Å from the top periodic boundary of the x−y plane in Figure 1 (blue-circled). Such a process is reproducible in other solvent systems, such as DME-DOL. The rearranged structure resembles a seesaw-shaped PF_4 coordinated with a rhombic Li_2F_2 complex. Throughout the P−F cleavage and rearrangement processes, chronological Bader charge analysis (see Figure S1 for details) indicates no charge variation occurring on neighbor electrolyte species or He; only Li and PF_6 clusters are involved in the charge transport without direct contact. Therefore, we suggest that such charge transfer-driven partial decomposition may be caused by electron tunneling from lithium metal to the dual-lithiated cation.

Moreover, such partial dissociation highly depends on the dual-lithium coordination to hexafluorophosphate and on the cluster charge state. Specifically, in the comparable configuration without extra "free" Li^+ available in the neighboring region of $LiPF_6$ or PF_6^-, the partial dissociation does not occur in the corresponding AIMD simulations. With dual lithiation, the P−F cleavage ceases after the $[Li_2PF_6]^+$ cluster receives an electron from Li metal and becomes negatively charged. We also compute Li^+ affinity energetics of different electrolyte species (Figure S2) and find that the lithiation free energies for the formation of $[Li_2PF_6]^+$ and [solvent-Li]$^+$ adduct are close to each other. Therefore, the population ratio of $[Li_2PF_6]^+$ cluster is equivalent to that of the solvated Li^+ in concentrated electrolytes. The $[Li_2PF_6]^+$ partial decomposition depicted above should be a non-negligible event during LMB fabrication.

We further analyze the Li-coordination's impacts on the electronic structure of $[PF_6]^x$ species. Previous studies have shown that lithiation reconstructs common electrolyte solvent molecules' HOMO and LUMO structures.[46,47] As suggested in Figure 2a,b, P−F bonding has strong covalency in PF_6^- anion

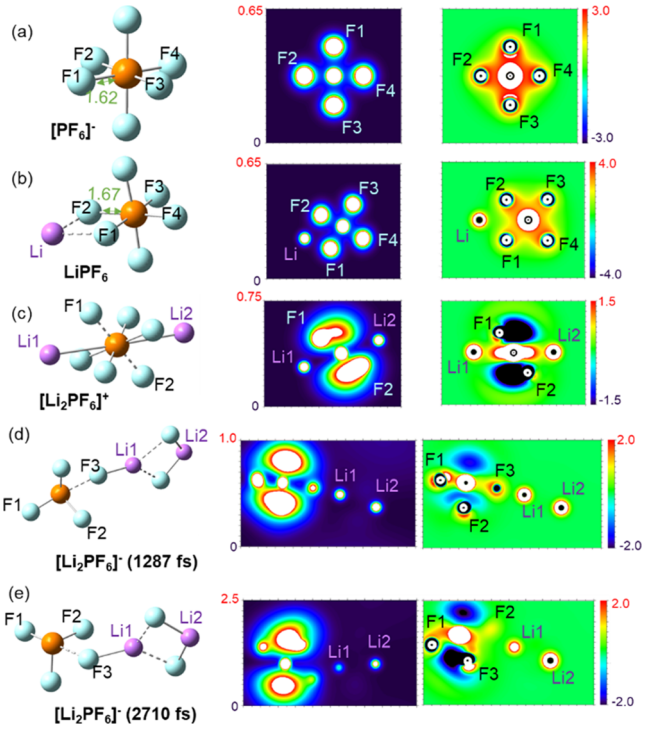

Figure 2. Geometry (left), electron density (middle), and electronic Laplacian (right) analysis of Li_2PF_6 clusters, including the optimized geometries of $[PF_6]^-$ (a) $LiPF_6$ (b), $[Li_2PF_6]^+$ (c), as well as the $[Li_2PF_6]^-$ structures (d, e) retrieved from AIMD simulations.[49] All of the electronic structure figures are plotted based on the planes determined by labeled atoms. Atomic color coding in structural geometries is identical to Figure 1. The rainbow color scale is labeled on the left (electron density) and right (Laplacian) sides of each diagram, where red indicates positive, and blue indicates zero/negative values.

and neutral $LiPF_6$ molecule, while the bond length is slightly extended due to the lithium coordination. When two lithium atoms are coordinated, some particular P−F bonds demonstrate ionic properties, as the electronic Laplacian planar plot indicates. The P−F distance (dashed bonds in 2d and 2e) also extends from 1.7 to 2.0 Å. Meanwhile, it is interesting to notice that the Li−P interaction shows positive Laplacian in the anionic cluster, suggesting covalent interactions between Li and P atoms, unlike the ionic Li−F cases. Therefore, high-level lithiation destabilizes the electronic configuration in $[PF_6]^x$ structure.

The semi-equilibrium geometry of $[Li_2PF_6]^x$ cluster, as described in Figures 1 and 2, is reproducible in AIMD simulations of both electrolyte systems of cyclic carbonate and ether solvents and is able to maintain its integrity within the feasible simulation time range (see Figures S1 and S3 for additional details). Based on Mulliken charge analysis of the two anionic $[Li_2PF_6]^-$ structures, the partial charges of Li_2F_2 moieties are generally neutral while the rest of the PF_4 substructures occupy most of the negative charge density (−0.83 and −0.87, respectively). Current computing power

https://doi.org/10.1021/acs.jpcc.2c07838
J. Phys. Chem. C 2023, 127, 1744−1751

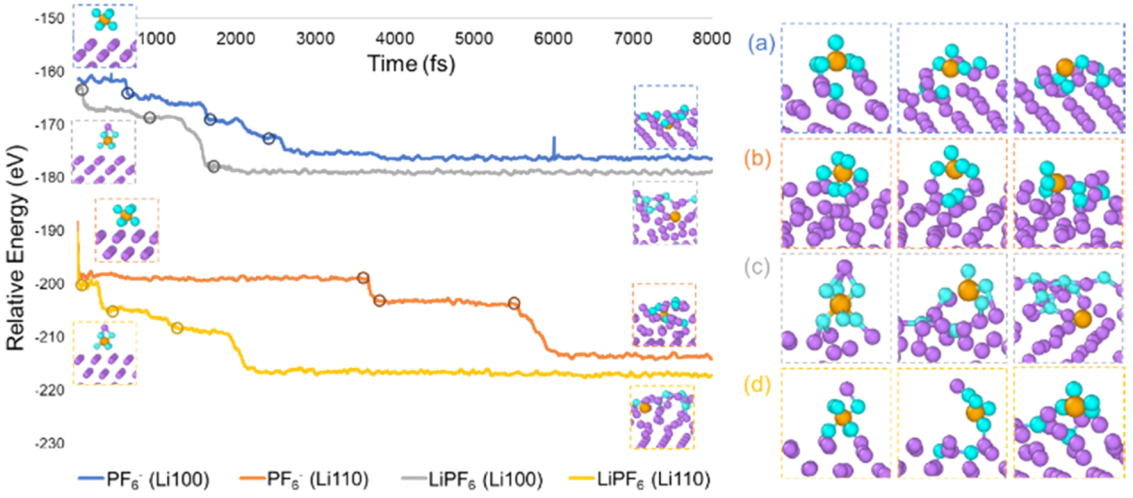

Figure 3. Energy profile of the hexafluorophosphate dissociation on different lithium metal facets retrieved from AIMD simulations. Important events are labeled with (a), (b), (c), and (d). The background charge of configurations (a) and (b) are both −1 e, while panels (c) and (d) are neutral. Atomic color coding is consistent with Figure 1.

limits AIMD from probing the final chemical forms of the partially dissociated $[Li_2PF_6]^x$ cluster. Over a longer time scale, such species may either (a) join undissociated PF_6^- anions and serve as ionic carriers in liquid electrolyte or (b) further decompose and become part of SEI. The close−shell $[PF_4]^-$ anion generated from Li1-F3 cleavage has a smaller diameter than the unreacted $[PF_6]^-$ and is thus expected to have a higher diffusion coefficient. From the battery electrolyte and SEI engineering perspective, the PF_6^- partial degradation near the anode material can lead to electrolyte ionic conductivity properties that differentiate from the direct measurement of pure $LiPF_6$ solution. Meanwhile, the electrolyte dielectric constant not only impacts the solvation of ionic species but also influences the electron transport rate from the metallic surface, determining the quantities of corresponding products.[25,48] For instance, it requires less than 1 ps in ether electrolytes (lower ε) to obtain the metastable $[Li_2PF_6]^-$ structure, while the equivalent process takes more than 2 ps in the carbonate system (higher ε). The Bader charge analysis of both systems (Figure S5) further confirms that such reductive dissociation results in significant charge variations on the lithium metal surface. Therefore, future LMB development could also benefit from the real-time analysis of electrolyte composition in working conditions.

Lithium Metal Surface Morphology. The lithium surface facet was found to be contributive to the electrolyte carbonate solvent defluorination thermodynamic pathways.[8] The surface Li−Li distances vary from 3.51 Å (100), 3.04 Å (110), to 4.96 Å (111), depending on the facets. The degradation energy profile of $LiPF_6$ also shows a significant mechanistic correlation with the regional metal surface structure.

We perform AIMD simulations on hexafluorophosphate species with different initial lithiation statuses. Background charge of opposite sign is applied to PF_6^--containing slabs (a) and (b) as no counter ion is included. Bader charge analysis of the initial configurations shows that the PF_6 clusters in both cases have −1.1 e equivalent charges, while lithium atoms representing bulk structures are generally neutral. Comparing Figure 3a−c,b−d, charge-neutral $LiPF_6$ demonstrates faster interfacial adsorption and dissociation than PF_6^- anion in equivalent Li facets. Mulliken charge analysis shows that lithium coordination "pushes" electron density to the fluorine atoms on the opposite side. In other words, the bare fluorine atoms are more electronegative than the Li-coordinated ones in a hexafluorophosphate cluster. The uneven internal charge distribution of $LiPF_6$ is mainly responsible for the increased degradation rate.

Based on the time required to reach comparable equilibrium, the hexafluorophosphate dissociation on Li(110) is slightly faster than that on Li(100), which has longer Li−Li distances. The first significant energy relaxation is a consequence of the hexafluorophosphate adsorption to the metal interface. Anionic hexafluorophosphate species can form more than four binding sites with the lithium metal surfaces before dissociation. When PF_6^- approaches the Li(100) surface, five F atoms simultaneously coordinate with neighboring Li atoms in 1 ps. PF_6^- maintains its geometric integrity longer until adsorbing to the Li(110) facet after approximately 3.5 ps. Comparatively, the charge-neutral $LiPF_6$ allows three fluorine atoms to bind with interfacial Li atoms upon adsorption. Thus, given the impact of salt concentration and solvent chemistry on the electrolyte structure at the Li metal/electrolyte interface, we expect that the observed significant chemical difference in the interactions of the anion with the surface highlighted here would influence the SEI properties derived from each electrolyte.

The differences in adsorption patterns result in the facet-dependency of fluorophosphate decomposition pathways. In Li(100) configurations, anionic PF_6^- experiences one-by-one sequential P−F bond cleavages (Figure 3a), while two fluorine atoms simultaneously cleave from the $LiPF_6$ structure (Figure 3c). A similar two-atom dissociation happens to PF_6^- on Li(110) (Figure 3b), while three fluoride anions leave the phosphorous center of $LiPF_6$ (Figure 3d). It is worth noting that at least two Li atoms are coordinated with the dissociated F atom in all of the dissociation events.

Based on our findings, anode metal surface modifications could be a rational strategy in SEI engineering. The Li−Li distances and surface charge distributions profoundly influence the SEI growing rate. Therefore, delicate modifications, including doping and chemical pretreatment, may tune the SEI to ideal structures and functional performance.[50]

https://doi.org/10.1021/acs.jpcc.2c07838
J. Phys. Chem. C 2023, 127, 1744−1751

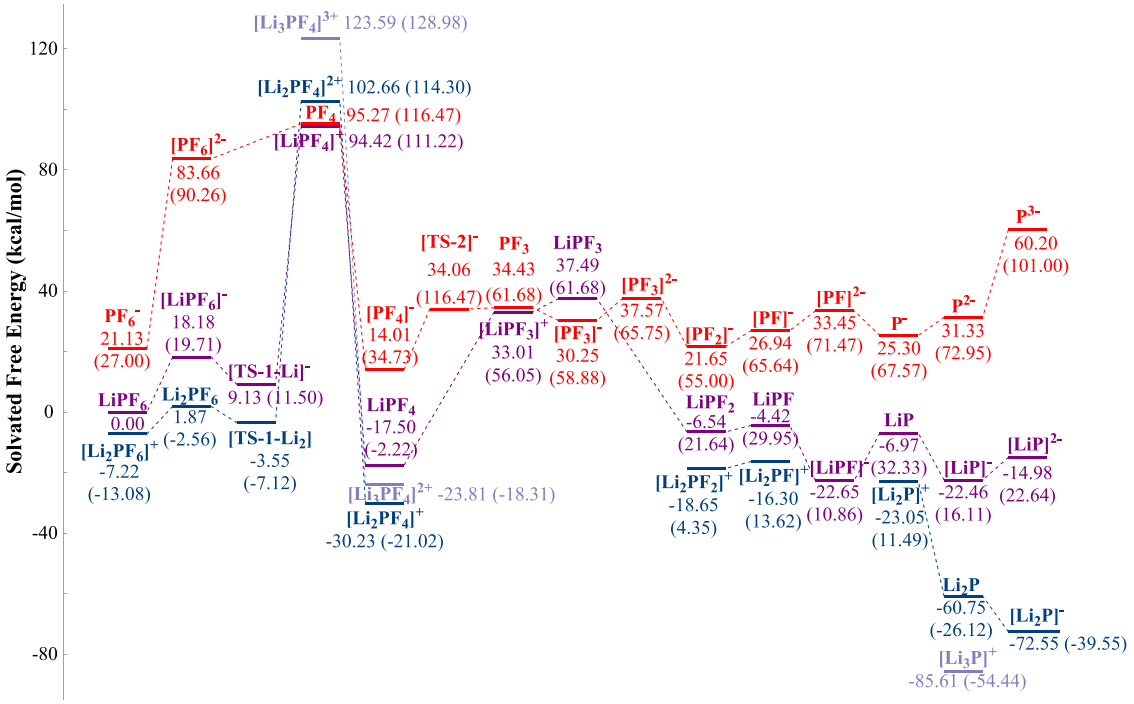

Figure 4. Free energy profile of $LiPF_6$ degradation computed in SMD (ε = 7.4). The red, purple, blue, and gray curves stand for nonlithiated, mono-lithiated, bi-lithiated, and tri-lithiated species, respectively. The relative free energies are labeled in kcal/mol, so are the enthalpy values in parenthesis.

Combined with the electronic structure evidence in the Introduction section, we can conclude that hexafluorophosphate degradation requires multiple (at least three) lithium coordinations to fluorine atoms. The semi-covalent Li−P interaction destabilizes P−F bonds and induces further charge transfer from nearby electron-rich lithium atoms. The accumulated negative charges further result in P−F bond cleavages. We compute the energy profile at the molecular level to quantitatively evaluate the impacts of lithiation and solvation in the decomposition pathway.

Hexafluorophosphate Degradation Pathway and Solvation's Role in Thermodynamic Profiles. To further understand the $LiPF_6$ decomposition reaction mechanism in the electrolyte, we investigate the energy profiles in different solvation systems. The Bader charge analysis of key time points in hexafluorophosphate degradation AIMD (Figures S3−S4 in the Supporting Information) demonstrates two necessary steps for P−F bond cleavages: (1) lithium coordination; (2) $[PF_x]^{y-}$ cluster receives external electron(s). Based on these criteria, we propose a plausible reaction mechanism that includes electron uptake followed by P−F bond cleavage. We also investigate the lithium bonding's thermodynamic role in such processes. In addition to the implicit SMD model, which mimics the DME-DOL electrolyte (Figure 4), we also obtain the free energy surface of the identical reaction pathway in higher dielectric constant and in gas-phase conditions shown in Figures S3 in the SI. Such a thermodynamic analysis of the primary SEI fluorination reaction in different solvation environments benefits a quantitative understanding of the reaction pathway and promotes rational electrolyte tuning in future work.

To model the complex solution−metal interfacial reactions, the relative energetics of each species are calculated with respect to $LiPF_6$, Li^+, Li(0), and F^- (Figure 4). This method provides rich information in understanding the stepwise energy barriers while being conservative in evaluating the exergonicity and exothermicity, especially when the generated particles embed into the solid surface. The largest free energy uphill is found at the electron-receiving step in forming the closed-shell PF_4 structures. Lithiation does not show any thermodynamic assistance in this step, while the thermochemistry is particularly favorable in the later reaction stages when more lithium cations bind with the intermediates. This is consistent with the AIMD finding that the dissociation progress is significantly faster after two P−F bonds are cleaved. Figure 4 shows that the nonlithiated pathway is unfeasible in the medium-dielectric environment, and the singly lithiated one is reluctant to proceed. The thermochemistry is generally favorable when at least two lithium atoms are coordinated. Therefore, the lithiation of $[PF_x]^{y-}$ intermediate induces charge transfer and plays an assistive role in P−F bond breaking.

We find that the transition states for P−F cleavages do not form significant thermodynamic obstacles; the electron uptake steps hinder the degradation instead. Note that compared with free energy, the enthalpy change in each stage is generally more positive/less negative, indicating that the dissociation progress is primarily entropy-driven. When the decomposition finishes and the initial SEI layer forms, the entropy reaches a local maximum. Besides the energy increase in generating the corresponding open-shell $[PF_x]^{y-}$ structures, charge transfer would be more sophisticated after the metallic surface is passivated.

We also assess solvation effects' role in hexafluorophosphate degradation. In the gas phase, where the dielectric constant is zero, the reaction shows a clear increasing trend in the free energy surface (Figure S6a). Such a pattern is completely inverted in high-dielectric-constant solvation conditions. As shown in Figure S6c, with a solvation environment comparable to the EC−VC electrolyte, the energy barrier for generating

https://doi.org/10.1021/acs.jpcc.2c07838
J. Phys. Chem. C 2023, 127, 1744−1751

PF_4 is significantly lower than that in DME-DOL. In addition, the following P−F dissociation steps are thermodynamically favorable in all of the lithiation conditions. The free energy uphill of all steps after generating the low-spin PF_4 species is significantly lower than the corresponding medium-dielectric scenario.

The solvation effects play two significant roles in the initial layer formation reactions of SEI. One is hindering direct electron tunneling between lithiated hexafluorophosphate species and lithium metal, and the other is creating a stabilizing solvation shell for intermediates in salt degradation. Thus, both the ionic conductivities and viscosity are altered together with the SEI formation kinetics and morphology when tuning the LMB liquid electrolyte. In the meantime, because the dissociation reaction rates are strongly correlated with the dielectric environment, people may rationally design the reagents for artificial SEI construction to control the ratios and distributions of different SEI components based on the criteria we present in this work.

CONCLUSIONS

This work showcases the complex chemical interactions among $LiPF_6$, electrolyte solvent, and lithium metal. The hexafluorophosphate structures that directly contact the Li metal surface easily experience further lithiation at the electrolyte−lithium−metal interface, where electrons are available for further reduction. The early-stage pathways and reaction rates of such interfacial dissociations are dependent on the regional lithium metal morphology. According to the continuum modeling, strong solvation effects and high lithiation degrees are assistive toward the decomposition thermochemistry. Energy barriers are flatter in a higher dielectric environment. In the solution phase, the electrolyte-dissolved hexafluorophosphate species is partially protected from complete degradation by limited lithiation and charge-transfer rates. Nonetheless, the dual-lithiated species $[Li_2PF_6]^+$ can still be incompletely reduced via electron tunneling without being adsorbed to the lithium surface. This partial decomposition is caused by elevated ionicity and destabilized electronic configurations of P−F bonding properties in the reduced and multilithiated structures.

The interfacial $LiPF_6$ degradation rate is associated with the porosity and density of the SEI initial layer. Techniques, including the surface modification for Li(110) facet exposure and pretreatments using high-dielectric $LiPF_6$-containing solutions, would benefit the formation of a dense LiF layer on lithium metal. The detailed mechanistic and thermodynamic information can be incorporated into coarse-grained kMC simulations for the understanding of SEI evolution processes on a larger time and length scale.

ASSOCIATED CONTENT

Supporting Information

The Supporting Information is available free of charge at https://pubs.acs.org/doi/10.1021/acs.jpcc.2c07838.

Details of charge distribution, atomic coordinates, energetics, etc. are available in the docx file. This information includes a stepwise free energy table for $LiPF_6$ dissociation; chronological Bader charge analysis of the electron-tunneling-induced $[Li_2PF_6]^+$ partial dissociation; lithium cation affinity energetics; Bader charge analysis of key AIMD frames of DME-DOL-solvated system; chronological Bader charge analysis of $[LiPF_6]$ and $[PF_6]^-$ interfacial degradations; significant events in forming metastable $[Li_2PF_6]^-$ structures in EC−VC and DME-DOL electrolytes; free energy profiles of LiPF6 decomposition in different implicit solvation environments; detailed energetics of species involved in LiPF6 decomposition pathways; and Cartesian coordinates of important structures (PDF)

AUTHOR INFORMATION

Corresponding Author

Perla B. Balbuena − *Department of Chemical Engineering, Texas A&M University, College Station, Texas 77843, United States; Department of Chemistry and Department of Materials Science and Engineering, Texas A&M University, College Station, Texas 77843, United States;* orcid.org/0000-0002-2358-3910; Email: balbuena@tamu.edu

Author

Dacheng Kuai − *Department of Chemical Engineering, Texas A&M University, College Station, Texas 77843, United States; Department of Chemistry, Texas A&M University, College Station, Texas 77843, United States;* orcid.org/0000-0002-4787-7331

Complete contact information is available at: https://pubs.acs.org/10.1021/acs.jpcc.2c07838

Author Contributions

The manuscript was written through contributions of all authors. All authors have given approval to the final version of the manuscript.

Funding

US Department of Energy Contract DE-AC02-05CH11357.

Notes

The authors declare no competing financial interest.

ACKNOWLEDGMENTS

The authors acknowledge the Assistant Secretary for Energy Efficiency and Renewable Energy, Office of Vehicle Technologies of the US Department of Energy, through the US-Germany Cooperation on Energy Storage under Contract DE-AC02-05CH11357. Computational resources from the Texas A&M University High Performance Research Computing are gratefully acknowledged. The valuable discussions with Dr. Ulrike Krewer and Janika Wagner are appreciated.

ABBREVIATIONS

SEI, solid electrolyte interphase; $LiPF_6$, lithium hexafluorophosphate; LMB, lithium metal battery; LiFSI, bis(fluorosulfonyl)imide; FEC, fluoroethylene carbonate; AIMD, ab initio molecular dynamics; DME, dimethoxyethane; DOL, 1,3-dioxolane; ε, dielectric constants; EC, ethylene carbonate; PC, propylene carbonate; VC, vinylene carbonate; MD, molecular dynamics; kMC, kinetic Monte Carlo; EDC, ethylene di-carbonate; SMD, solvation model based on density; PBE, Perdew−Burke−Ernzerhof; GGA, generalized gradient approximation; PAW, projector augmented wave

REFERENCES

(1) Choi, J. W.; Aurbach, D. Promise and Reality of Post-Lithium-Ion Batteries with High Energy Densities. *Nat. Rev. Mater.* **2016**, *1*, No. 16013.

(2) Wang, H.; Yu, Z.; Kong, X.; Kim, S. C.; Boyle, D. T.; Qin, J.; Bao, Z.; Cui, Y. Liquid Electrolyte: The Nexus of Practical Lithium Metal Batteries. *Joule* **2022**, *6*, 588−616.
(3) He, X.; Bresser, D.; Passerini, S.; et al. The Passivity of Lithium Electrodes in Liquid Electrolytes for Secondary Batteries. *Nat. Rev. Mater.* **2021**, *6*, 1036−1052.
(4) Jang, E. K.; Ahn, J.; Yoon, S.; Cho, K. Y. High Dielectric, Robust Composite Protective Layer for Dendrite-Free and Lipf6 Degradation-Free Lithium Metal Anode. *Adv. Funct. Mater.* **2019**, *29*, No. 1905078.
(5) Peled, E.; Menkin, S. Review—SEI: Past, Present and Future. *J. Electrochem. Soc.* **2017**, *164*, A1703−A1719.
(6) Yu, Z.; Rudnicki, P. E.; Zhang, Z.; et al. Rational Solvent Molecule Tuning for High-Performance Lithium Metal Battery Electrolytes. *Nat. Energy* **2022**, *7*, 94−106.
(7) Li, Y.; Li, Y.; Pei, A.; et al. Atomic Structure of Sensitive Battery Materials and Interfaces Revealed by Cryo-Electron Microscopy. *Science* **2017**, *358*, 506−510.
(8) Zhang, Y.; Viswanathan, V. Not All Fluorination Is the Same: Unique Effects of Fluorine Functionalization of Ethylene Carbonate for Tuning Solid-Electrolyte Interphase in Li Metal Batteries. *Langmuir* **2020**, *36*, 11450−11466.
(9) Hobold, G. M.; Lopez, J.; Guo, R.; Minafra, N.; Banerjee, A.; Shirley Meng, Y.; Shao-Horn, Y.; Gallant, B. M. Moving Beyond 99.9% Coulombic Efficiency for Lithium Anodes in Liquid Electrolytes. *Nat. Energy* **2021**, *6*, 951−960.
(10) Tarascon, J. M.; Armand, M. Issues and Challenges Facing Rechargeable Lithium Batteries. *Nature* **2001**, *414*, 359−367.
(11) Kuai, D.; Balbuena, P. B. Solvent Degradation and Polymerization in the Li-Metal Battery: Organic-Phase Formation in Solid-Electrolyte Interphases. *ACS Appl. Mater. Interfaces* **2022**, *14*, 2817−2824.
(12) Shi, S.; Lu, P.; Liu, Z.; Qi, Y.; Hector, L. G., Jr.; Li, H.; Harris, S. J. Direct Calculation of Li-Ion Transport in the Solid Electrolyte Interphase. *J. Am. Chem. Soc.* **2012**, *134*, 15476−15487.
(13) Zhang, Z.; Li, Y.; Xu, R.; et al. Capturing the Swelling of Solid-Electrolyte Interphase in Lithium Metal Batteries. *Science* **2022**, *375*, 66−70.
(14) Qian, Y.; Hu, S.; Zou, X.; et al. How Electrolyte Additives Work in Li-Ion Batteries. *Energy Storage Mater.* **2019**, *20*, 208−215.
(15) Yu, Y.; Karayaylali, P.; Katayama, Y.; Giordano, L.; Gauthier, M.; Maglia, F.; Jung, R.; Lund, I.; Shao-Horn, Y. Coupled Lipf6 Decomposition and Carbonate Dehydrogenation Enhanced by Highly Covalent Metal Oxides in High-Energy Li-Ion Batteries. *J. Phys. Chem. C.* **2018**, *122*, 27368−27382.
(16) Kuai, D.; Cheng, H.; Kuan, K.-Y.; Yan, X. Accelerated Five-Component Spiro-Pyrrolidine Construction at the Air−Liquid Interface. *Chem. Commun.* **2021**, *57*, 3757−3760.
(17) Yao, N.; Chen, X.; Fu, Z.-H.; Zhang, Q. Applying Classical, Ab Initio, and Machine-Learning Molecular Dynamics Simulations to the Liquid Electrolyte for Rechargeable Batteries. *Chem. Rev.* **2022**, *122*, 10970−11021.
(18) Dhattarwal, H. S.; Kuo, J.-L.; Kashyap, H. K. Mechanistic Insight on the Stability of Ether and Fluorinated Ether Solvent-Based Lithium Bis(Fluoromethanesulfonyl) Electrolytes near Li Metal Surface. *J. Phys. Chem. C.* **2022**, *126*, 8953−8963.
(19) Yamijala, S. S. R. K. C.; Kwon, H.; Guo, J.; Wong, B. M. Stability of Calcium Ion Battery Electrolytes: Predictions from Ab Initio Molecular Dynamics Simulations. *ACS Appl. Mater. Interfaces* **2021**, *13*, 13114−13122.
(20) Martinez de la Hoz, J. M.; Soto, F. A.; Balbuena, P. B. Effect of the Electrolyte Composition on Sei Reactions at Si Anodes of Li-Ion Batteries. *J. Phys. Chem. C.* **2015**, *119*, 7060−7068.
(21) Galvez-Aranda, D. E.; Seminario, J. M. Li-Metal Anode in a Conventional Li-Ion Battery Electrolyte: Solid Electrolyte Interphase Formation Using Ab Initio Molecular Dynamics. *J. Electrochem. Soc.* **2022**, *169*, No. 030502.
(22) Yao, N.; Chen, X.; Shen, X.; Zhang, R.; Fu, Z.-H.; Ma, X.-X.; Zhang, X.-Q.; Li, B.-Q.; Zhang, Q. An Atomic Insight into the Chemical Origin and Variation of Dielectric Constant in Liquid Electrolytes. *Angew. Chem., Int. Ed.* **2021**, *60*, 21473−21478.
(23) Ren, X.; Zou, L.; Jiao, S.; et al. High-Concentration Ether Electrolytes for Stable High-Voltage Lithium Metal Batteries. *ACS Energy Lett.* **2019**, *4*, 896−902.
(24) Jiao, S.; Ren, X.; Cao, R.; et al. Stable Cycling of High-Voltage Lithium Metal Batteries in Ether Electrolytes. *Nat. Energy* **2018**, *3*, 739−746.
(25) Rostkier-Edelstein, D.; Urbakh, M.; Nitzan, A. Electron Tunneling through a Dielectric Barrier. *J. Chem. Phys.* **1994**, *101*, 8224−8237.
(26) Chen, X.; Zhang, Q. Atomic Insights into the Fundamental Interactions in Lithium Battery Electrolytes. *Acc. Chem. Res.* **2020**, *53*, 1992−2002.
(27) Lu, D.; Shao, Y.; Lozano, T.; et al. Failure Mechanism for Fast-Charged Lithium Metal Batteries with Liquid Electrolytes. *Adv. Energy Mater.* **2015**, *5*, No. 1400993.
(28) Ospina-Acevedo, F.; Guo, N.; Balbuena, P. B. Lithium Oxidation and Electrolyte Decomposition at Li-Metal/Liquid Electrolyte Interfaces. *J. Mater. Chem. A* **2020**, *8*, 17036−17055.
(29) Perez Beltran, S.; Balbuena, P. B. Sei Formation Mechanisms and Li+ Dissolution in Lithium Metal Anodes: Impact of the Electrolyte Composition and the Electrolyte-to-Anode Ratio. *J. Power Sources* **2022**, *551*, 232203−232210.
(30) Spotte-Smith, E. W. C.; Kam, R. L.; Barter, D.; Xie, X.; Hou, T.; Dwaraknath, S.; Blau, S. M.; Persson, K. A. Toward a Mechanistic Model of Solid−Electrolyte Interphase Formation and Evolution in Lithium-Ion Batteries. *ACS Energy Lett.* **2022**, *7*, 1446−1453.
(31) Kresse, G.; Hafner, J. Ab Initio Molecular Dynamics for Liquid Metals. *Phys. Rev. B* **1993**, *47*, 558−561.
(32) Perdew, J. P.; Burke, K.; Ernzerhof, M. Generalized Gradient Approximation Made Simple. *Phys. Rev. Lett.* **1996**, *77*, 3865−3868.
(33) Blöchl, P. E. Projector Augmented-Wave Method. *Phys. Rev. B* **1994**, *50*, 17953−17979.
(34) Kresse, G.; Joubert, D. From Ultrasoft Pseudopotentials to the Projector Augmented-Wave Method. *Phys. Rev. B* **1999**, *59*, 1758−1775.
(35) Ehrlich, S.; Moellmann, J.; Reckien, W.; Bredow, T.; Grimme, S. System-Dependent Dispersion Coefficients for the Dft-D3 Treatment of Adsorption Processes on Ionic Surfaces. *ChemPhysChem* **2011**, *12*, 3414−3420.
(36) Tang, W.; Sanville, E.; Henkelman, G. A Grid-Based Bader Analysis Algorithm without Lattice Bias. *J. Phys.: Condens. Matter* **2009**, *21*, No. 084204.
(37) Dunning, T. H., Jr. Gaussian Basis Sets for Use in Correlated Molecular Calculations. I. The Atoms Boron through Neon and Hydrogen. *J. Chem. Phys.* **1989**, *90*, 1007−1023.
(38) Woon, D. E.; T, H. D., Jr. Gaussian Basis Sets for Use in Correlated Molecular Calculations. Iii. The Atoms Aluminum through Argon. *J. Chem. Phys.* **1993**, *98*, 1358−1371.
(39) Han, J.; Zheng, Y.; Guo, N.; Balbuena, P. B. Calculated Reduction Potentials of Electrolyte Species in Lithium−Sulfur Batteries. *J. Phys. Chem. C* **2020**, *124*, 20654−20670.
(40) Marenich, A. V.; Cramer, C. J.; Truhlar, D. G. Universal Solvation Model Based on Solute Electron Density and on a Continuum Model of the Solvent Defined by the Bulk Dielectric Constant and Atomic Surface Tensions. *J. Phys. Chem. B* **2009**, *113*, 6378−6396.
(41) Grimme, S.; Antony, J.; Ehrlich, S.; Krieg, H. A Consistent and Accurate Ab Initio Parametrization of Density Functional Dispersion Correction (Dft-D) for the 94 Elements H-Pu. *J. Chem. Phys.* **2010**, *132*, No. 154104.
(42) Wang, Y.; Nakamura, S.; Ue, M.; Balbuena, P. B. Theoretical Studies to Understand Surface Chemistry on Carbon Anodes for Lithium-Ion Batteries: Reduction Mechanisms of Ethylene Carbonate. *J. Am. Chem. Soc.* **2001**, *123*, 11708−11718.
(43) Wang, Y.; Nakamura, S.; Tasaki, K.; Balbuena, P. B. Theoretical Studies to Understand Surface Chemistry on Carbon Anodes for

https://doi.org/10.1021/acs.jpcc.2c07838
J. Phys. Chem. C 2023, 127, 1744−1751

Lithium-Ion Batteries: How Does Vinylene Carbonate Play Its Role as an Electrolyte Additive? *J. Am. Chem. Soc.* **2002**, *124*, 4408−4421.
(44) Leung, K.; Budzien, J. L. Ab Initio Molecular Dynamics Simulations of the Initial Stages of Solid−Electrolyte Interphase Formation on Lithium Ion Battery Graphitic Anodes. *Phys. Chem. Chem. Phys.* **2010**, *12*, 6583−6586.
(45) Borodin, O.; Olguin, M.; Spear, C. E.; Leiter, K. W.; Knap, J. Towards High Throughput Screening of Electrochemical Stability of Battery Electrolytes. *Nanotechnology* **2015**, *26*, No. 354003.
(46) Chen, X.; Li, H.-R.; Shen, X.; Zhang, Q. The Origin of the Reduced Reductive Stability of Ion−Solvent Complexes on Alkali and Alkaline Earth Metal Anodes. *Angew. Chem., Int. Ed.* **2018**, *57*, 16643−16647.
(47) He, J.; Wang, H.; Zhou, Q.; Qi, S.; Wu, M.; Li, F.; Hu, W.; Ma, J. Unveiling the Role of Li^+ Solvation Structures with Commercial Carbonates in the Formation of Solid Electrolyte Interphase for Lithium Metal Batteries. *Small Methods* **2021**, *5*, No. 2100441.
(48) Winkler, J. R.; Gray, H. B. Long-Range Electron Tunneling. *J. Am. Chem. Soc.* **2014**, *136*, 2930−2939.
(49) Lu, T.; Chen, F. Multiwfn: A Multifunctional Wavefunction Analyzer. *J. Comput. Chem.* **2012**, *33*, 580−592.
(50) Fu, L. J.; Liu, H.; Li, C.; Wu, Y. P.; Rahm, E.; Holze, R.; Wu, H. Q. Surface Modifications of Electrode Materials for Lithium Ion Batteries. *Solid State Sci.* **2006**, *8*, 113−128.

https://doi.org/10.1021/acs.jpcc.2c07838
J. Phys. Chem. C 2023, 127, 1744−1751